Diamond-based structures to collect and guide light

To cite this article: S Castelletto *et al* 2011 *New J. Phys.* **13** 025020

New Journal of Physics
The open-access journal for physics

Diamond-based structures to collect and guide light

S Castelletto[1,5], J P Harrison[2], L Marseglia[2,5], A C Stanley-Clarke[2], B C Gibson[3], B A Fairchild[3], J P Hadden[2], Y-L D Ho[2], M P Hiscocks[4], K Ganesan[3], S T Huntington[3], F Ladouceur[4], A D Greentree[3], S Prawer[3], J L O'Brien[2] and J G Rarity[2]

[1] Centre for Micro-Photonics, Faculty of Engineering and Industrial Sciences, Swinburne University of Technology, Mail H 34 Hawthorn, VIC 3122, Australia
[2] Centre for Quantum Photonics, H H Wills Physics Laboratory and Department of Electrical and Electronic Engineering, University of Bristol, Merchant Venturers Building, Woodland Road, Bristol BS8 1UB, UK
[3] School of Physics, The University of Melbourne, Melbourne VIC 3010, Australia
[4] School of EE&T, University of New South Wales, Sydney, NSW 2052, Australia
E-mail: scastelletto@swin.edu.au and luca.marseglia@bristol.ac.uk

New Journal of Physics **13** (2011) 025020 (24pp)
Received 17 August 2010
Published 21 February 2011
Online at http://www.njp.org/
doi:10.1088/1367-2630/13/2/025020

Abstract. We examine some promising photonic structures for collecting and guiding light in bulk diamond. The aim of this work is to optimize single photon sources and single spin read-out from diamond color centers, specifically NV^- centers. We review the modeling and fabrication (by focused ion beam and reactive ion etching) of solid immersion lenses, waveguides and photonic crystal cavities in monolithic diamond.

[5] Author to whom any correspondence should be addressed.

Contents

1. Introduction

Diamond has emerged in recent years as a unique platform for quantum communication [1] and spin qubit operations [2, 3], as well as for 'quantum imaging' based on single spin magnetic resonance [4] or nanoscopy [5]. Impressive demonstrations in all these areas have mostly been based on the negatively charged nitrogen vacancy center (NV^-), which consists of a substitutional nitrogen atom adjacent to a carbon vacancy. Due to its exceptional optical and magnetic spin selection properties, NV^- has been used to demonstrate a stable single photon source [6] and single spin manipulations [7]–[9] at room temperature. A single photon source based on NV^- in nano-diamond is already commercially available [10], and a ground state spin coherence time of 15 ms has been observed in ultra-pure diamond at room temperature [11]. At present, one of the biggest issues preventing diamond from taking the lead among competing technologies (e.g. quantum dots [12]) is the difficulty in fabricating photonic devices to couple and guide light. This is due to the extreme hardness, high refractive index and poor electrical conductivity of diamond. For the realization of large-scale quantum information processing protocols (e.g. via photonic module approaches [13]) or for quantum repeater systems, it will be necessary to connect NV^- centers through 'flying' qubits such as photons. To achieve this, micro-cavities and waveguides are needed to enable the transfer of quantum information between the electron spin of the NV^- center and a photon.

The objective of the research presented here is to optimize the output coupling of photons from diamond color centers into waveguides and free space to increase the efficiency of single photon sources and to enable faster single spin read-out. In this paper, we concentrate on fabrication strategies to sculpt photonic structures in bulk diamond material, which is expected to give rise to the highest-quality quantum-diamond systems. There are at least two reasons why bulk diamond is preferred. Firstly, the quality of the emitters is greater due to the reduced defect and impurity concentration, and increased distance to interfaces that give rise to dephasing. Secondly, the optical properties are improved due to a lack of interface scattering and access to the bound modes of the light guiding structures. However, to realize the vision of monolithic diamond quantum devices requires the generation of a complete nanofabrication toolkit for diamond and diamond color centres. Here we report on some new techniques towards realizing this toolkit. Alternatives to monolithic approaches often employ nano-manipulation techniques to place nano-crystal diamonds into existing photonic crystal structures or onto fiber

tips [14]–[17]. We also note here other hybrid approaches where NV^- centers, either in nano-diamond or single-crystal diamond, have been coupled to gallium phosphide (GaP) waveguides, silica micro-spheres and GaP micro-discs [18]–[21].

Two conceptually distinct classes of coupling structures are the subject of this paper. The first class is non-resonant collecting structures. Solid immersion lenses are in this class and can deliver surprisingly high collection efficiencies when optimally configured. We discuss the modeling of such lenses and then present experimental results from lenses fabricated using a focused ion beam (FIB) etching technique. We also discuss a waveguide realization directly in single-crystal diamond based on photo-lithography, reactive ion etching (RIE) and FIB milling [22]. It is relevant to mention that within this category diamond nanowires of 200 nm width and 2 μm length have recently been produced by electron-beam lithography and RIE in single-crystal diamond, yielding an improvement of collection efficiency from an NV^- center with respect to bulk diamond [23].

The second class is resonant confining structures. These confine the light close to the emitter allowing cavity-QED effects to be exploited to direct an emitted photon into a particular spatial mode. The performance of defect centers can be strongly enhanced through coupling to an optical micro-cavity. An improvement of the photon emission rate and photon indistinguishability for NV^- can be achieved due to the (coherent) interaction with the highly localized photon field of the cavity [24]. There have been considerable advances with hybrid resonator approaches, leveraging mature photonic fabrication approaches. These include the coupling of NV^- centers to moderate-Q silicon nitride cavities [16], to on-chip micro-cavities [20] and to high-Q micro-cavities [20, 25]. In addition, a theoretical demonstration of the use of slot waveguides in diamond to highly confine and guide the light in an ultra-small cavity modal volume [26] shows an alternative, although challenging, path for cavity-QED with diamond centers.

Monolithic diamond is ultimately more desirable than hybrid approaches, and high-Q micro-cavities have been designed for diamond [27]–[30]. However, the first experimental demonstrations with micro-disc resonators [31] and photonic crystal cavities [32] suffered large scattering losses due to the poly crystal nature of the diamond material used. The fabrication of high-Q cavities in single-crystal diamond is very challenging because vertical optical confinement within diamond requires either a three-dimensional etching process or a method for fabricating thin single-crystal diamond films [33]. We will analyze photonic crystal structures in diamond and fabrication methods to achieve efficient spin read-out in low-Q cavities [34].

2. Non-resonant collecting structures

2.1. Solid immersion lenses

Efficient photon collection from color centers in bulk diamond is frustrated by the relatively high refractive index (2.42) of the material. At the diamond–air interface the angle for total internal reflection (TIR) is $\sim 25^\circ$. This means that for a microscope objective with a numerical aperture (NA) of 0.9, the overall maximum collection efficiency from a planar diamond surface is a few per cent at best. It is possible to overcome TIR by using nano-crystals; indeed a 50% increase in collection efficiency over bulk diamond has been measured for NV^- emission in nano-diamonds [35]. However, for scalability in quantum information applications the use of

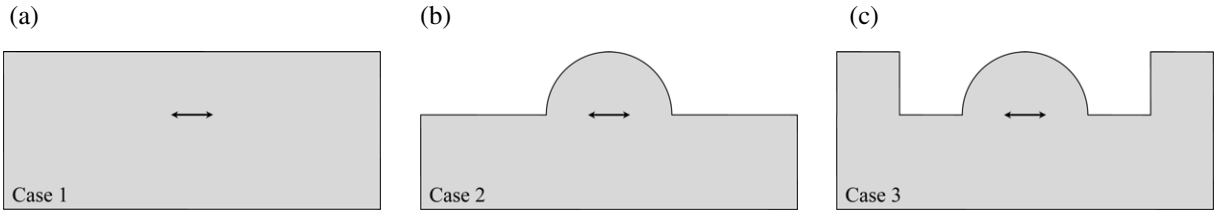

Figure 1. The three cases modeled in our finite-difference time-domain (FDTD) simulations, as reported in [43]. In all cases the dipole direction is taken to be in the plane of the slab. (a) Dipole 2.5 μm below the planar diamond surface. (b) Dipole at the focus of the 5 μm diameter hemisphere. (c) Dipole at the focus of the 5 μm diameter hemisphere surrounded by a 2 μm wide trench.

bulk material is preferable, particularly given the recent progress towards creating single NV^- centers in bulk diamond with adequate spatial control [36]–[38].

A conceptually simple solution to the problem of TIR is to have the emitter at the focal point of a hemispherical lens (figure 1(b)). This type of optic is called a solid immersion lens (SIL). The use of a solid 'immersion' material was first demonstrated by Mansfield and Kino [39] to improve the resolution in a scanning optical microscope system. Apart from the obvious advantage of not freezing at cryogenic temperatures, solid materials can have a refractive index far in excess of the best immersion oils. SILs made from high refractive index glass have been used to improve the efficiency of collecting photoluminescence from quantum wells [40], and effective NAs as high as 2 have been reported for (GaP) SILs [41], and more recently a ZrO_2 SIL has been coupled to an NV^- center [42]. These are impressive results but, for the purpose of integration, an SIL created directly in diamond is more desirable than a free-standing optical component.

Below we present the results of simulations for calculating the maximum collection efficiency achievable for a single NV^- center in an integrated diamond SIL. We then discuss the experimental results achieved with SILs fabricated in polycrystal diamond.

2.1.1. Simulations. To simulate the collection efficiency in an objective lens with NA = 0.9, we used an FDTD method. We calculated the collection efficiencies for an NV^- center located 2.5 μm below a planar surface (figure 1(a)), at the focal point of a hemisphere of 5 μm diameter (figure 1(b)) and at the focal point of a hemisphere surrounded by a 2 μm wide trench (figure 1(c)). In all cases the NV^- center dipole is oriented parallel to the diamond surface. The SIL-with-trench case is included as a simple way of approximating an ideal SIL using FIB fabrication. Simulated collection efficiencies over the spectral range of NV^- emission for the three cases are shown in figure 2. Taking an average over the spectral range, we calculate collection efficiencies of 5.2, 29.8 and 28.6% for cases 1, 2 and 3, respectively. In the first two cases, the collection efficiency can be calculated analytically. For a dipole, the intensity at a point (θ, ϕ), where θ and ϕ are defined in the usual way for spherical coordinates, is given by [44]

$$I(\theta, \phi) = \frac{3}{8\pi}[1 - \sin^2\theta \cos^2\phi]. \quad (1)$$

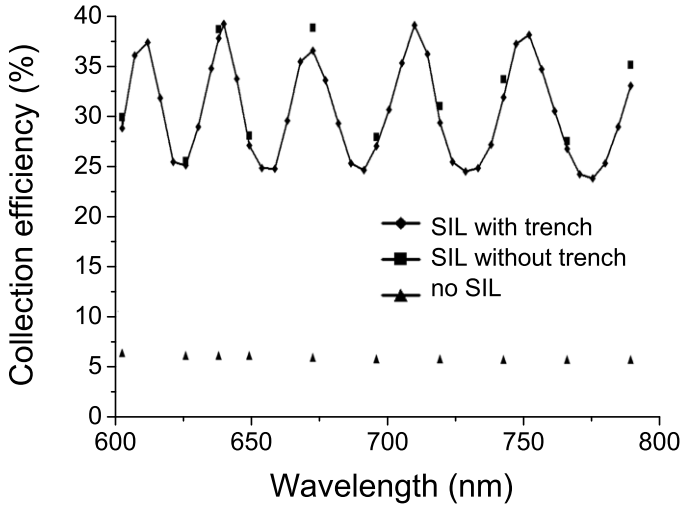

Figure 2. Wavelength dependence of the collection efficiency (into a 0.9 NA objective) for the three cases modeled in FDTD simulations.

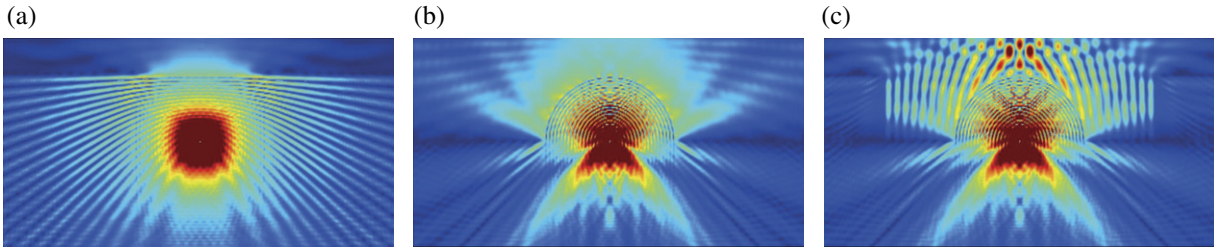

Figure 3. Electromagnetic field intensity (red indicates high intensity) calculated from FDTD simulations [43]. (a) Dipole in a planar slab of diamond. (b) Dipole at the focus of the hemisphere. (c) Dipole at the focus of the hemisphere with a trench.

Using Snell's law to determine the maximum internal angle and integrating over the NA, the collection efficiency, η, is given by

$$\eta = \frac{1}{32}\left[15\left(1-\sqrt{1-\left(\frac{\mathrm{NA}}{n}\right)^2}\right)+\left(1-\cos\left[3\arcsin\left(\frac{\mathrm{NA}}{n}\right)\right]\right)\right], \tag{2}$$

where n is 1 with an SIL and 2.42 (the refractive index of diamond) with no SIL. The collection efficiencies calculated in this way are 5.28 and 32.62%. These are slightly higher than those obtained in our numerical calculation and this is to be expected for two reasons. First, reflection at the diamond–air interface is included in the FDTD simulations, but not in the analytic case. A more subtle effect can be seen in the collection efficiency data and in the electromagnetic field plots (figure 3) produced by the FDTD simulations. A periodic modulation of the field intensity in the forward direction is seen when an SIL is present (figures 3(b) and (c)). The modulation is due to reflections from the SIL boundary acting to modify the dipole emission in the backward direction. The oscillations in the plot of collection efficiency as a function of wavelength (figure 2) arise because the collection efficiency is defined as the emission through

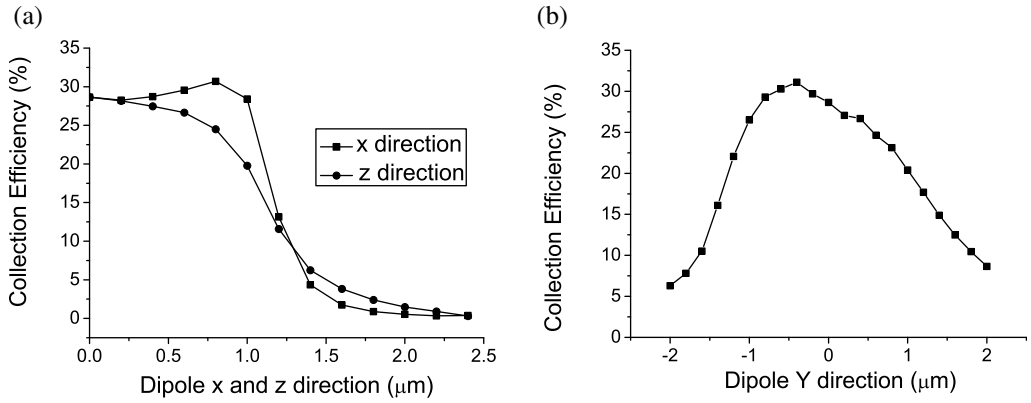

Figure 4. Change in collection efficiency as the dipole position is moved from the focal point of the hemisphere. Note that the collection efficiency is a smooth function of the misalignment and optimal coupling is slightly displaced from the focal point of the SIL due to the fact that the emitter is a dipole and therefore not spherically symmetric. (a) Change in collection efficiency as the NV^- is moved along the x- or z-axis with $y = 0$. (b) Change in collection efficiency as the NV^- is moved along the y-axis for $x = z = 0$.

the SIL (which remains roughly constant) normalized by the total emission in all directions (which oscillates). With this in mind, it is worth noting that oscillations in the plot of collection efficiency as a function of wavelength (figure 2) are real and are a consequence of this quantum interference effect.

By confirming that our FDTD simulation agrees with Snell's law in the ideal case of a dipole positioned exactly at the focal point of the SIL, we can be confident about our model when considering non-ideal cases where an analytic solution is not available. A comparison between cases 2 and 3 is useful to check that the simplest structure to fabricate (case 3) results in a collection efficiency that is close to the ideal case (case 2), so more complicated fabrication is not necessary. However, what we are most interested in is how the SIL performance varies when the dipole position deviates from the focal point of the hemisphere. To investigate this we simulated moving the dipole in all three dimensions (dipole emission is toroidal, so the two lateral planes are not symmetric). The change in collection efficiency as a function of position along each axis is shown in figure 4. It should be noted that the lateral directions are assigned as x and z here, and the longitudinal as y. It can be seen in figure 4(b) that a 1 μm error in the dipole height, in either direction, reduces the collection efficiency to 25%. Sensitivity to dipole position is similar in both of the lateral directions (figure 4(a)). In other words, our SIL fabrication process needs to be accurate to about 1 μm to avoid a significant loss in efficiency.

2.1.2. Fabrication. Fabrication of SILs in ultra-pure single-crystal diamond (Element Six) was carried out using a 30 keV focused gallium-ion beam system (FEI Strata FIB-201). To approximate a hemisphere, a series of concentric rings of increasing depth and diameter were milled. Beam currents ranged from 70 to 11 500 pA, and water-assisted etching was used to maximize the removal of etch products. Figure 5 shows images of the SILs taken using secondary electron emission in the FIB system. The ultra-pure diamond material has

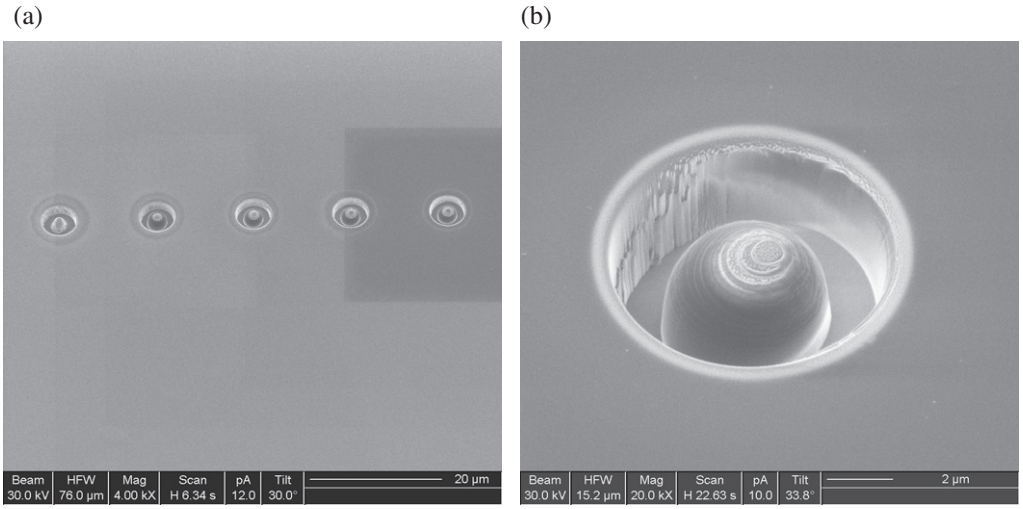

Figure 5. FIB images of SILs in ultra-pure diamond. (a) An array of 5 μm diameter SILs fabricated in ultra-pure single-crystal diamond using FIB etching. (b) Close-up image of one SIL.

an extremely low density of intrinsic fluorescent defects, so SILs fabricated in this material showed no sign of NV^- center emission, but from a visual inspection of the images it is clear that high-quality hemispherical structures can be made.

2.1.3. Measurement of single-color centers under SILs. To find centers under these structures, several SILs were also fabricated 'randomly' in polycrystalline diamond material with a moderate density of intrinsic single NV^- centers. A few of these SILs were found to contain a single NV^- center and an enhancement factor (compared to single NV^- emission from the planar bulk material) as high as 10 has been measured [43]. This enhancement factor exceeds that calculated in the FDTD simulations in section 2.1.1, but this is not unexpected since significant spherical aberrations from bulk diamond will also affect the collection efficiency and such aberrations are eliminated in the SIL. Figure 6(a) shows a confocal image of a 2.5 μm radius SIL containing a single NV^- center, while figure 6(b) shows a comparison of intensity saturation curves for a single NV^- center under an SIL compared to one in an un-etched part of the sample clearly showing the enhanced collection. Full details of these results have been published [43].

Having successfully found single NV^- centers by chance, this work has now been extended to the study of ultra-pure diamond implanted with an ordered array of NV^- centers. It has recently been shown that a single NV^- center can be fully characterized and its position marked to 100 nm precision. Subsequent fabrication of an SIL above the center has been demonstrated with collection enhancement factor up to six [45].

In a similar way, defects emitting in the near-infrared region formed by the implantation of chromium have been studied [46, 47] and marked. Preliminary measurements show that the SIL registering technique can be applied to these samples, and enhanced collection efficiency is at present under evaluation.

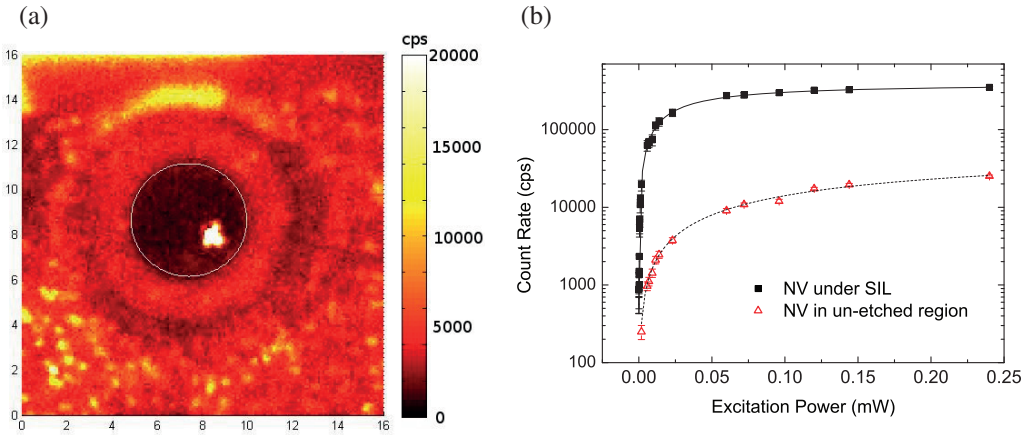

Figure 6. (a) Confocal fluorescence image of a single NV^- center inside an SIL. A circle has been added to indicate the perimeter of the SIL. It should be noted that the color scale has been adjusted so that the bright NV^- center is 'over-exposed' in order to make the trench around the SIL clearer. (b) Photon count rate (corrected for background) as a function of excitation power for an NV^- center inside an SIL and a typical NV^- center in the un-etched region.

2.2. Diamond waveguides

To obtain long-range qubit–qubit interaction of NV^- centers, high-efficiency photon collection and routing is needed. Again, focusing on monolithic on-chip solutions, here we show progress towards diamond waveguides. We discuss the fabrication of ∼200 nm membranes in diamond and two alternative methods for creating waveguides in monolithic diamond: FIB milling and RIE. FIB is an excellent method for making one-off devices to prototype and explore the potential of a material. However, RIE is aligned with the imperatives of scalable e-beam production processes and is ultimately the method that we see as being the most important for diamond devices.

Freestanding waveguide structures have been created in thin (3.5 μm) layers of diamond by combining an implantation process with a single-energy ion irradiation and lift-out technique. This enabled the fabrication of active structures of the order of 80 μm long with a cross-section of $3.5 \times 2\ \mu m^2$ [48]. However, these dimensions are substantially larger than those required for single-mode propagation of NV^- zero-phonon line photons ($\sim 200 \times 200\ nm^2$ for a square core diamond–air waveguide). Our ultimate goal is to make single-mode waveguides and cavities with tailored optical centers incorporated into diamond membranes.

An alternative fabrication process is based on creating two graphitic layers with a thin diamond membrane (200 nm) sandwiched between them by using two irradiation energies [33]. This procedure allows the desired layer to be at greater depth, where the ion-induced damage threshold is higher, and it is possible to anneal the diamond at higher temperature without graphitizing or damaging the layers of interest. However, milling layers with these dimensions involves overcoming technical challenges. To implement fabrication procedures relying on milling thin layers of diamond to reach the desired single-mode sizes, we tested methods for protecting the diamond from stray ion beam damage, as discussed in section 2.2.2.

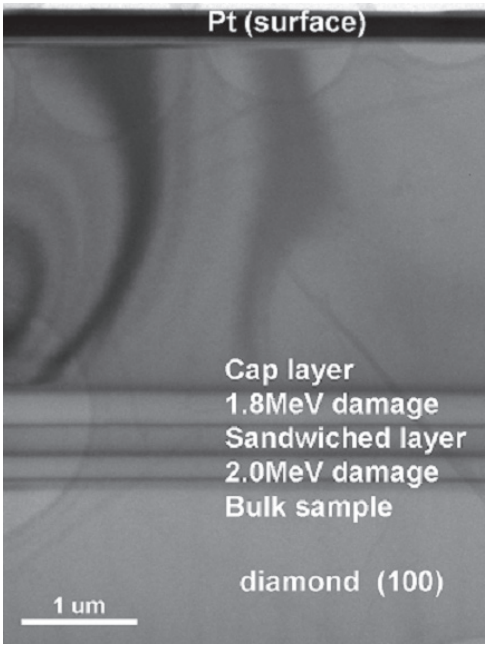

Figure 7. TEM image of a single-crystal diamond and amorphous carbon zones. The sample is implanted and the cap layer and damage zones from 1.80 and 2.00 MeV helium ions are indicated. The 2.00 MeV ions are implanted first, with the lower energy ions implanted afterwards [33].

An alternative method to FIB milling is RIE and we believe this method has significant advantages for large-scale manufacture of devices. We fabricated waveguide structures in HPHT type 1b single-crystal diamond (Sumitomo) using photolithography and RIE, discussed in section 2.2.3. The combination of these techniques allows the patterning of many long photonic structures simultaneously, improving scalability. Moreover, this technology can be realistically pushed to single-mode operation and is more compatible with current opto-electronic processing.

2.2.1. Fabrication of 200 nm layers in a single-crystal diamond. The lift-out method reported in [48] cannot be scaled to generate sub-micron layers due to the limits of ion implantation and cracking due to stress. To overcome these limitations, a double-implantation (sandwich) technique was developed [33], realizing single-crystal membranes of the order of 200 nm thickness and $300 \times 300\,\mu m^2$ area. Here we briefly review this method which we believe is an enabling process for device fabrication.

Our method is based on a lift-off method developed by Parikh *et al* [49] and utilizes the increased damage threshold for amorphization available at depth. The critical dose, or damage threshold, D_c, at the surface has been established as 1×10^{22} vacancies cm^{-3} [50]. However, several authors [51, 52] have indicated that this value is higher at depth. Initial results indicated that the layer of material that converts to graphite-like material was only 100–300 nm upon annealing at 800 °C.

The significance of a narrow layer of damage at depth is demonstrated in figure 7, which shows the presence of amorphous regions at 3.1 and 3.5 μm from 1.8 and 2.0 MeV helium ions,

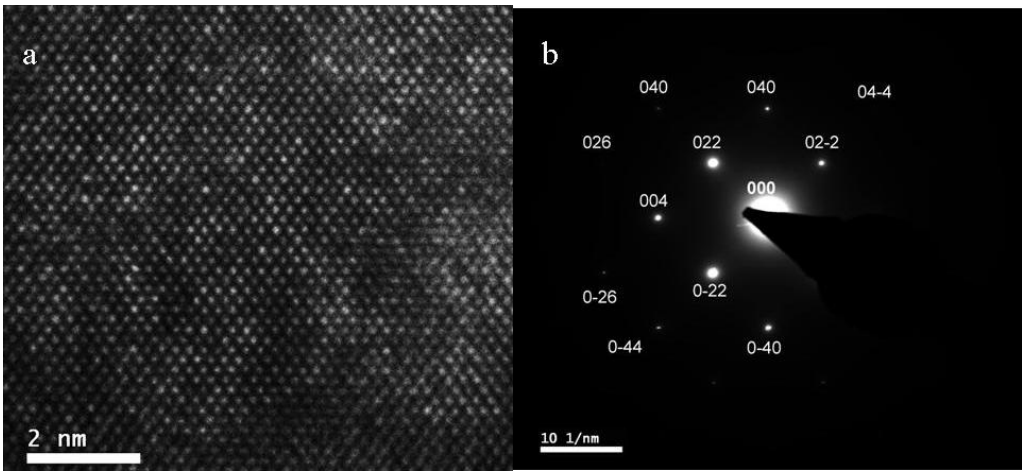

Figure 8. (a) High-resolution TEM image of the as-implanted diamond layer before annealing and etching. (b) Diffraction image from the diamond membrane after lift-out, with all spots indexed to single-crystal diamond. Reproduced with permission from [33]. © Wiley-VCH Verlag GmbH.

respectively. This combination of ion implantations produced a diamond layer of 350 nm, and by reducing the difference in implantation energies an even thinner layer could be produced. Using this method [33], we fabricated 660, 330, 250 and 210 nm layers of single-crystal diamond.

The quality of the resulting membrane can be seen in the high-resolution transmission electron microscopy image of the $\langle 1, 1, 0 \rangle$ lattice planes in figure 8(a), and in the TEM diffraction pattern for a 330 nm layer that matches the expected pattern for a single-crystal diamond (figure 8(b)).

Annealing in vacuum at temperatures $>1100\,^{\circ}$C transforms the amorphous layer to graphite, which becomes a sacrificial layer. By etching this region, an undercut is created that can provide vertical confinement for photonic applications. As the temperature increases up to 1400 °C the interface between the diamond and graphite regions becomes sharper. Investigating this interface and its properties will be the focus of further study.

2.2.2. FIB milling of waveguiding structures. Milling in diamond layers of the order of 200 nm thickness poses significant technical challenges that must be solved before this scheme can be considered a viable and scalable technology. As the layer becomes thinner, and structures narrower, they are more susceptible to low-level damage from scattered ions during milling. Indeed all FIB cuts are also vulnerable to widening at the top of the cut, as shown by [53]–[55], due to sputtering of ions from the base of the cuts being made. In thick layers with large structures, the degradation caused by these stray ions and broadening of cuts is not so critical. However, as the structure size decreases, the impact of this unintended damage becomes more significant and far more care is needed in the fabrication of thin layers than for thicker test samples. Figures 9(a) and (b) show that as the cross-section of the optical structure approaches single-mode dimensions, the amount of damaged material below the milled surface (shown in gray in figure 9(b)) becomes more significant and may render the device non-functional.

To refine fabrication methods approaching these single-mode dimensions, test structures were fabricated. Layers of single-crystal diamond of the order of 0.9 μm were used as the

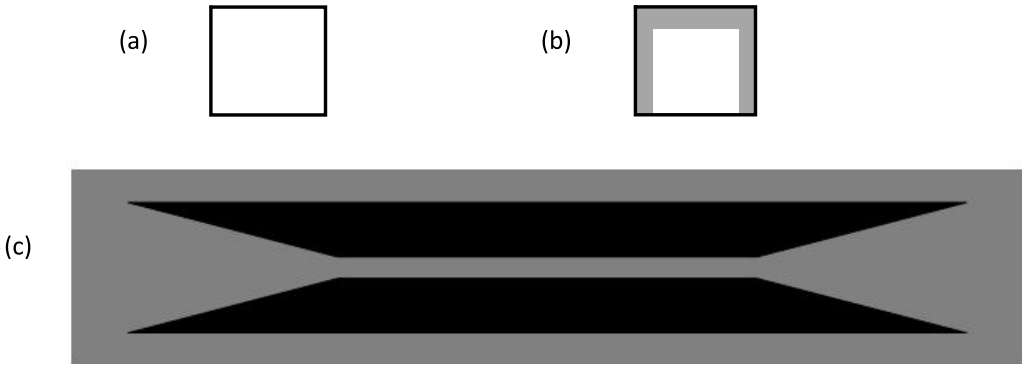

Figure 9. (a) Cross-section of an ideal waveguide. (b) Cross-section of an actual waveguide, showing FIB damage from vertical cuts ≈20 nm thick and damage to the surface layer from stray Ga ions during milling 20–50 nm. (c) The bitmap pattern used to define the milling and area for a tapered waveguide. The black region is the intended region to be milled, the gray-shaded region is the area affected by stray ions.

starting point for our investigations. The thin layer is produced from a single-energy, 0.5 MeV implantation of He ions using similar methods to [56]. We made several waveguide structures in the resulting layers and report some of our findings below.

Milling of the waveguide structure in the FIB is controlled by using a bitmap to define milled and non-milled regions. The black region in figure 9(c) shows the bitmap that sharply defines the area to be milled. However, the milling beam (30 keV gallium) is not as well defined as the map suggests, and stray ions can affect a large region, shaded gray. In addition, the electronic blanking used to move or shut off the gallium beam can leave a dusting of ions over the scanned area, which can be visible in both optical and SEM images. The effect of low doses of gallium damage on the refractive index of diamond is also being studied [57]. Effects due to stray ions can be overcome by depositing a sacrificial layer (of platinum, for example) 50–400 nm thick on the surface of the sample. This thickness is sufficient to absorb any stray ion implantation from the FIB and is easily milled in regions where cuts are intended (i.e. the black regions of figure 9(c)). While this technique is common in TEM sample preparation [58], its use for optical devices is uncommon. In our case, complete removal of the platinum layer is essential for device operation. The platinum layer must be thick enough to stop all unintended exposure of the membrane surface by gallium ions.

A sacrificial platinum mask also plays a significant role in improving the quality of the milled structures. The gallium beam mills the material by sputtering ions from the surface. This can lead to the rounding of edges, or broadening, of the cut at the surface where a right angle cut would be preferred. This is shown in figure 10, with figure 10(a) showing the ideal FIB cuts and figure 10(b) the broadening of cuts near the surface due to sputtering. Figure 10(c) shows a layer of sacrificial platinum thick enough to ensure the absorption of scattered ions (typically 20 nm for 30 keV gallium ions in diamond). By making the sacrificial platinum layer thicker, 200–300 nm, this region of widening of a cut can occur in the platinum layer rather than in the membrane layer of interest. The depth of the platinum layer can be adjusted to allow for widening of cuts, which can extend to hundreds of nm depending on the depth of the cut or the focus of the gallium beam.

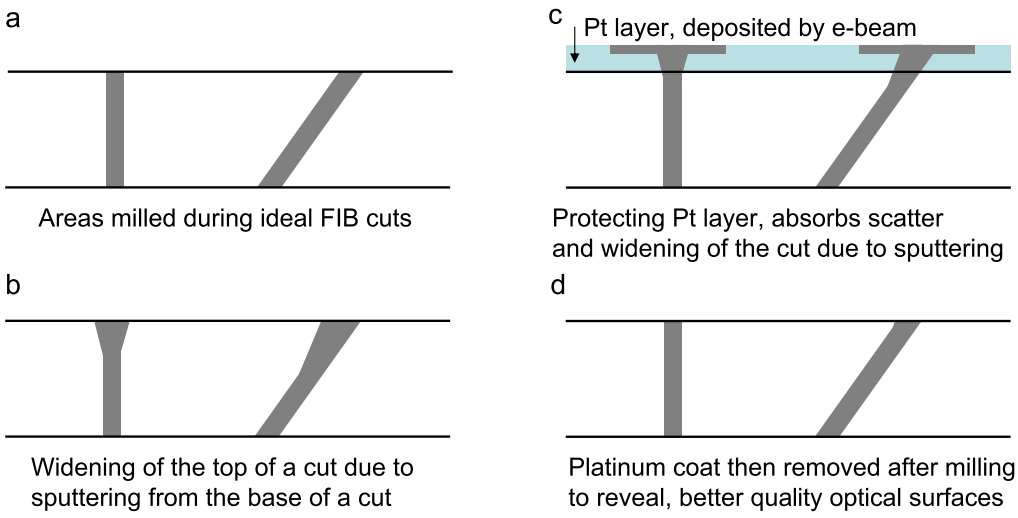

Figure 10. A schematic view of FIB milled cuts. (a) Ideal cuts without broadening and/or stray ion damage. (b) The broadening of cuts caused by material being sputtered from the base of the cut. (c) A platinum layer deposited on the surface of the optical layer to protect regions near the intended cuts. The damage to the top surface from stray ions of the Gaussian gallium beam is shown by the horizontal dark gray-shaded areas. (d) After the removal of platinum, the resultant cuts show significantly less broadening at the surface.

Control of the depth of the platinum layer is especially important for mirror cuts. Mirror cuts are particularly vulnerable to broadening at the surface, since the material is thinner on one side at the top of the cut. Broadening at the surface of mirror cuts changes the resulting angle of the mirror and lowers the surface area of the final mirror as shown in figure 10(b), reducing the coupling efficiency. While mirror length loss is not significant in thicker layers with mirrors 3–6 μm long, using a 1 μm input spot size, the resulting loss of intensity for a 200 nm layer where the mirror is of the order of 300 nm long is significant. Therefore the loss of mirror length in sub-micron layers can render the device ineffective. Once milling is complete, the sacrificial platinum layer can be removed, revealing cuts that are closer to the ideal case as shown in figure 10(d). By removing the metal protecting layer, this method is significantly different from the standard TEM preparation method, and only with its complete removal to expose the undamaged diamond surface can the full optical properties of the device be realized.

The techniques described here were used to fabricate waveguides with a cross-section of $0.9 \times 1.0\,\mu m^2$, tapered length 115 μm, with mirrors 135 μm apart. Figure 11(a) shows the structure in transmitted light, post-FIB milling but with the platinum layer still in place. The platinum layer is seen as dark since it blocks the light path and the milled cuts are transparent so that the waveguide can be seen in outline. Figure 11(b) shows the sample after the platinum layer has been removed by boiling in oxidizing acids. Optical characterization of these waveguides was performed as described in section 2.2.4.

2.2.3. The RIE fabrication process. In this section, we review in detail some results reported in [22, 59] obtained by this technique.

The waveguide structures were fabricated in type 1b single-crystal diamond (Sumitomo). Before the RIE protocol (shown schematically in figure 12) was carried out, a sacrificial

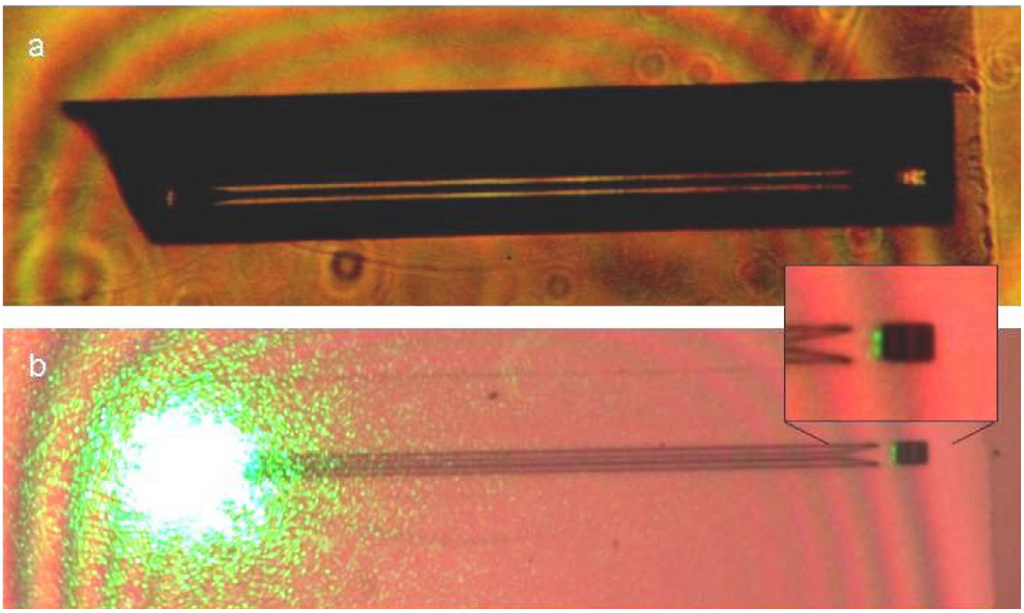

Figure 11. A waveguide with a cross-section of $0.9 \times 1.0\,\mu\text{m}^2$, tapered length $115\,\mu\text{m}$ with mirrors $135\,\mu\text{m}$ apart. (a) A transmitted light image of the waveguide with the platinum layer (dark) still present and the waveguide visible inside it. (b) The same structure after the platinum layer has been removed, showing a multi-mode output on the output mirror, shown in zoom for clarity.

graphitic layer was created as described above, at a depth of $3.5\,\mu\text{m}$ by He ion implantation and subsequent annealing. The first step in the RIE protocol was to deposit a layer of silica $\sim$400 nm thick on the sample using plasma-enhanced chemical vapor deposition. This layer acts as the mask when etching the diamond [31]. The sample was then dehydration-baked and exposed to hexamethyldisilazane to promote the adhesion of the photoresist. AZ6112 photoresist was spin-deposited onto the sample, resulting in a layer approximately $1.2\,\mu\text{m}$ thick at the center. Relative to standard silicon wafers, diamond single crystals have a small surface area and a large height, which makes them more difficult to process. When spinning the photoresist onto the sample, not all of the crystal surface was covered uniformly due to edge effects. The resist pattern was etched into the silica mask using RIE with CF_4 and Ar gases at an RF power of 100 W and a pressure of 10 Pa. Once the silica mask was etched through, the underlying diamond was then etched in a predominantly oxygen plasma with a small amount of CHF_3 at 200 W and a pressure of 10 Pa. The etch rate was found to be $\sim 70\,\text{nm}\,\text{min}^{-1}$, with good selectivity.

Figure 13 shows an optical microscope reflection image of the surface of the diamond sample once it has gone through the photolithography and RIE process outlined above. The waveguides shown do not extend to the edges of the crystal, due to the edge effects mentioned in the preceding paragraph. For standard silicon wafers these regions are usually cleaved off, but this is not practical when processing diamond. The patternable area was still large enough to create seven ridge waveguide structures, with lengths ranging from $\sim$1.5 to 2.5 mm, which can be seen running horizontally in figure 13. Figures 14(a) and (b) are SEM images of one of these ridge waveguide structures. Figure 14(a) is a top view and shows that the width at the top of the ridge is $5.05\,\mu\text{m}$. The two lighter, slightly charged, sections of the waveguide are the sidewalls

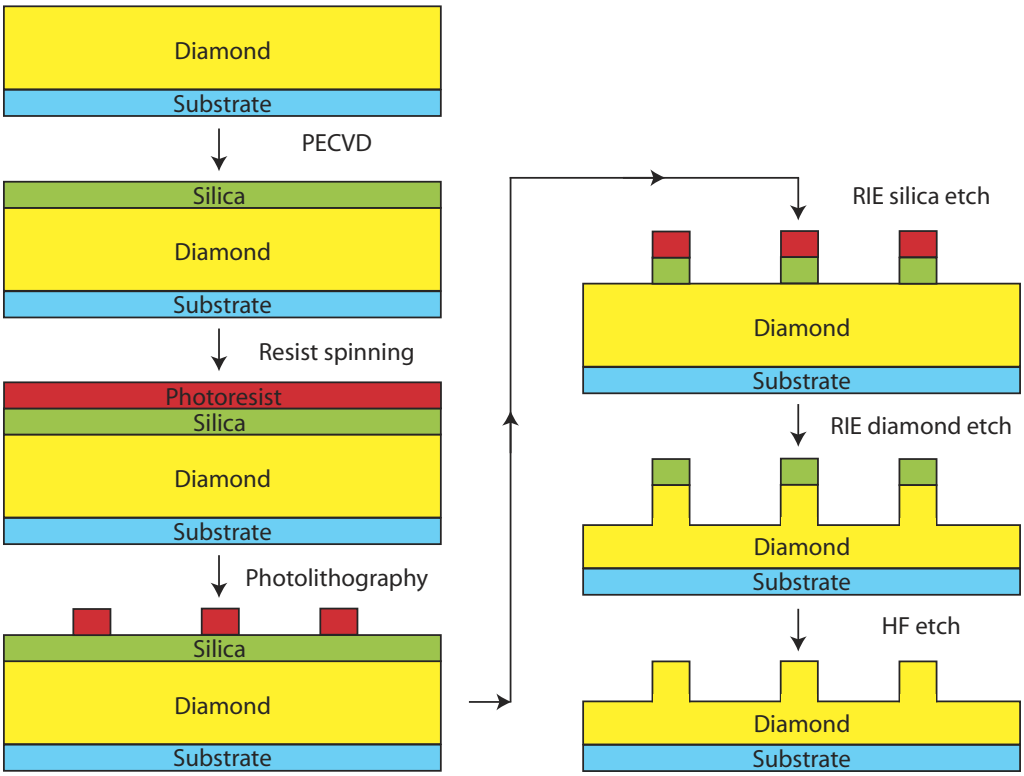

Figure 12. RIE process flowchart detailing the masking, etching and release of the final ridge waveguide structure. For monolithic structures, the substrate is also diamond, and needs to be released from the ridge structure via a sacrificial layer as detailed in section 2.2. The use of RIE and photo- or e-beam lithography is essential for the creation of scalable devices.

of the ridge. The areas on the left and right sides of the ridge are the unmasked regions where the diamond was removed by the RIE process. Raman spectroscopy of these etched regions showed no change in the Raman shift relative to that of the pristine sample, which indicates that the quality of the diamond post-RIE is not degraded. The etch depth for this sample was 1.15 μm and an atomic force microscope (AFM) measurement of a 1.1 μm $\times$ 1.6 μm surface area gave an rms roughness of 2.7 nm for the etched region. A larger AFM measurement over an area of 2 μm $\times$ 4 μm gave an rms roughness of 5.0 nm for the top of the ridge. A magnified section of the left side of the ridge is shown in figure 14(b). The majority of the sidewall shows a peak-to-peak roughness of less than 10 nm. The roughness is larger at the base of the ridge, although it is still only $\sim$20 nm peak-to-peak. This result is comparable to the best sidewall roughness results obtained for diamond across all combinations of patterning and etching techniques [60, 61].

As a result of the waveguides not extending to the edges of the diamond crystal, TIR mirrors, as shown in figure 16, were used to launch light into, and collect light from, the waveguides [48]. An FIB of 30 keV Ga^+ ions was used to make 45° mirrors. The FIB was also used to mill holes through the upper diamond layer to gain access to the 3.5 μm deep sacrificial graphitic layer. An electrochemical etch was then used to etch the graphite from beneath the waveguides, leaving an air gap to provide vertical confinement for the waveguiding structure.

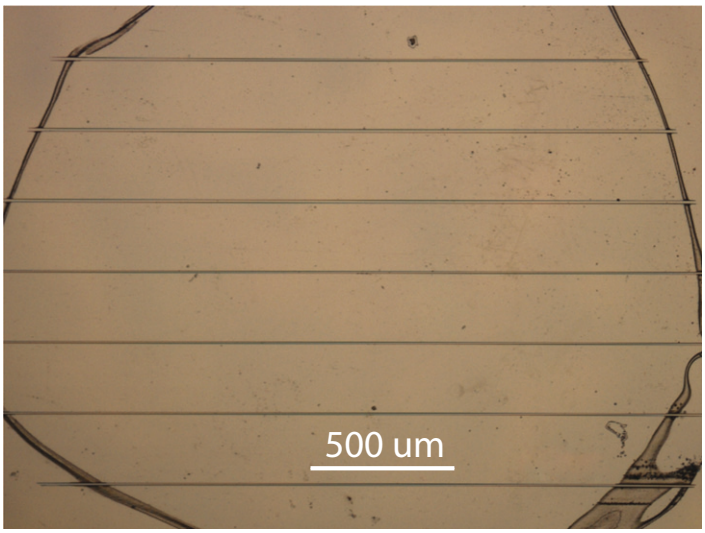

Figure 13. Optical microscope reflection image of the surface of the reactive ion-etched sample. Seven ridge waveguide structures can be seen running horizontally across the sample. The waveguides range in length from approximately 1.5 to 2.5 mm with a RIE depth of 1.15 μm. Reproduced with permission from [59]. © Elsevier (2008).

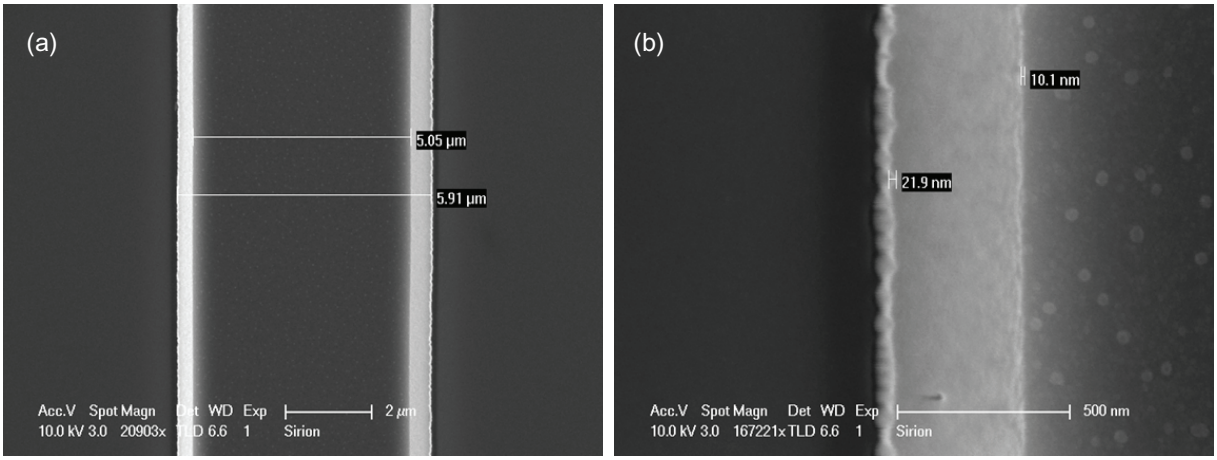

Figure 14. (a) Ridge structure etched in a single-crystal diamond. Etch depth = 1.15 μm. (b) Magnified image of the ridge sidewall. Reproduced with permission from [59]. © Elsevier (2008).

Transmission and reflection optical microscope images of the electrochemically etched sample, with the FIB milled holes indicated, are shown in figures 15(a) and (b), respectively.

2.2.4. Optical characterization. The system used to optically characterize the RIE-diamond ridge waveguide structures and the FIB milled structures is shown schematically in figure 16. A 532 nm laser was focused to a μm-sized spot at the input TIR mirror using a long-working-distance 50× magnification objective lens. The transmitted light from the output

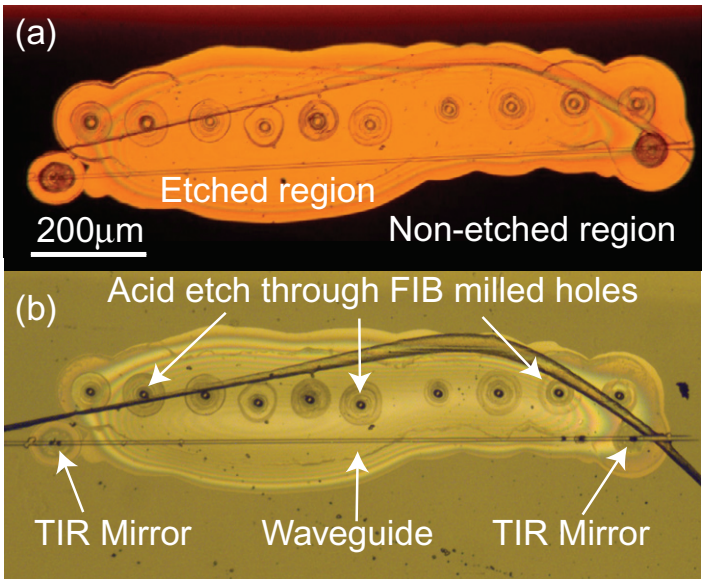

Figure 15. Optical microscope images of the waveguide with graphite etched from beneath the structure. (a) A transmission image; (b) a reflection image. Both the image widths are ∼1 mm [22].

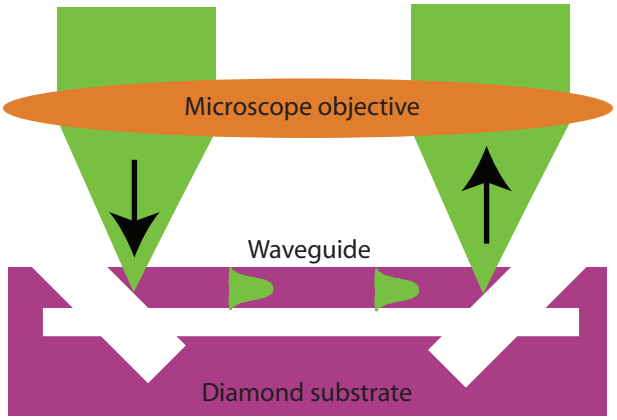

Figure 16. Schematic diagram of the input waveguide coupling and output light-collection system that uses TIR mirrors [22].

mirror was collected with the same objective lens. This scheme limits the field of view of the coupling/collection setup to about 100 μm. Therefore, to validate whether optical guidance could be achieved in RIE-diamond structures, two 45° mirrors were milled at either end of a waveguide with a length of about 80 μm. The dimensions of the core, or 'ridge', part of the waveguide were approximately 5 μm wide × 1.15 μm high. The propagation of light in the RIE-diamond ridge waveguide device was investigated and the waveguiding results are shown in figures 17(a)–(d). Light was coupled into the waveguide through the TIR mirror on the left side of figures 17(a) and (b) and the modal output of the waveguide was observed on the right-hand side of each image. The multimode intensity pattern observed at the output mirror clearly indicates that the waveguide is coupling light. Variation of the input beam position is

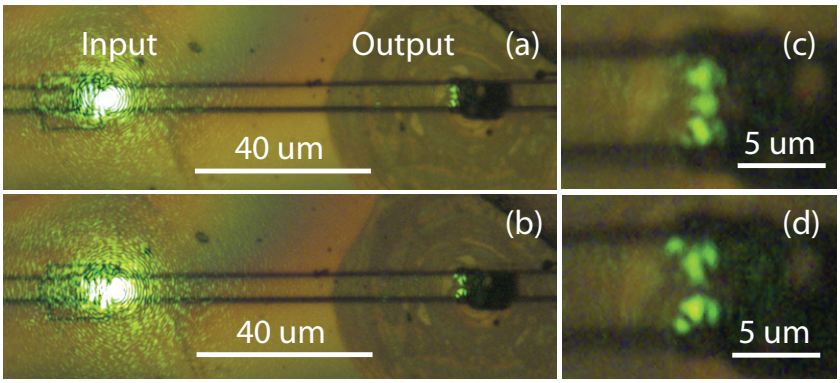

Figure 17. Panels (a) and (b) show an 80 μm section of the waveguide with light coupling in through the left-hand side mirror and the multimode output from the mirror on the right-hand side. Panels (c) and (d) show a magnified image of the mode pattern on the output mirror of panels (a) and (b), respectively [22].

responsible for the different mode patterns observed in figures 17(a) and (b). Magnified images of the waveguide output (figures 17(c) and (d)) appear to show a combination of at least the fundamental and second-order modes.

3. Resonant confining structures

3.1. Photonic crystals

To take advantage of strong atom–photon coupling using NV^-, as required by many of the most advanced quantum protocols, cavity structures are required. Again, concentrating on monolithic diamond solutions, photonic crystal cavities are the most natural structures to explore, although slot cavity structures have also been considered [26]. Zero-phonon emission, at 637 nm, accounts for only a small fraction ($\sim$4% at liquid helium temperature) of NV^- fluorescence, with the majority of emitted photons falling in the very broad ($\sim$200 nm) phonon-assisted sideband. By coupling the NV^- center to a photonic crystal cavity, spontaneous emission in the phonon sideband can be suppressed and emission in the zero-phonon line can be enhanced [24].

A photonic crystal structure modulates the propagation of light in a way that is analogous to a semiconductor crystal modulating the motion of electrons. In both cases a periodic structure gives rise to 'band-gap' behavior, with a photon (electron) being allowed or not allowed to propagate depending on its wave vector. In photonic crystals the periodicity is comprised of regions of higher and lower dielectric constants. The period needs to be of the order of a half-wavelength of the light to be confined, i.e. a few hundred nanometers for visible wavelengths [62]. The challenges of engineering diamond at this scale are not trivial, as described in section 2.2.1.

High-Q resonators of different kinds have been fabricated in non-diamond materials and coupled to NV^- emission from nano-diamonds (see for example [16, 20]). Since we are concerned here with developing monolithic photonics, it is necessary to fabricate cavities in the diamond itself. It should be noted that photonic crystal cavities have been fabricated in nano-diamond films and an un-coupled Q-factor as high as 585 at 637 nm was measured [32]. The polycrystal nature of the material used in those demonstrations makes it unsuitable for

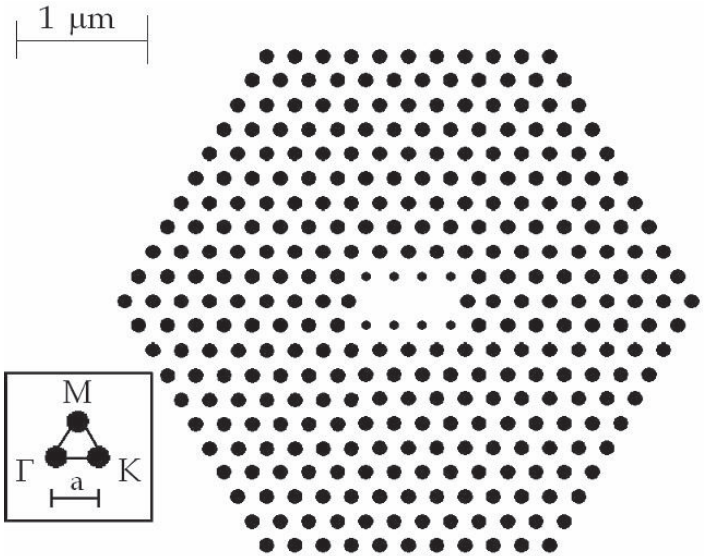

Figure 18. L3 'Noda' photonic crystal cavity.

our purposes due to enhanced scattering and background fluorescence. In this work, we aim to fabricate photonic crystal cavities in ultra-high-purity type IIa single-crystal diamond (Element Six) grown by chemical vapor deposition. This material has extremely low levels of nitrogen (less than 1 ppb), and very few native NV^- centers, making it the ideal material for creating NV^- centers in a controlled fashion by implantation and annealing.

Strong coupling and entanglement require high-Q cavities, but a cavity with a more moderate Q would still be useful. In particular, a scheme for reading out the ground state spin of an NV^- center has been described that requires a Q (before coupling) of only $\sim$3000 [34]. This scheme exploits the zero-field splitting in the NV^- center ground state and uses narrow band resonant excitation to achieve high-fidelity read-out of the ground state spin with just a few excitation cycles.

To realize this read-out scheme, we chose a structure known as a 'Noda' cavity, illustrated schematically in figure 18 and described in detail in section 3.1.1. For a complete analysis of this structure, see [63]. It is sufficient here to note that confinement in the out-of-plane direction arises from TIR at the crystal–air interface, while in-plane confinement is achieved by exploiting the photonic band-gap behavior of the structure.

3.1.1. Simulations. As can be seen in figure 18, the photonic crystal consists of a hexagonal array of air holes in a slab of diamond. To ensure single-mode operation at some wavelength λ, a slab thickness of $\sim\lambda/4$ is required [62]. The cavity itself is formed by three missing holes in the center. An FDTD method was used to simulate the behavior of the cavity. The parameters that can be varied to optimize the performance of the cavity are the lattice constant, a, the radius of the air holes and the slab thickness. The air holes adjacent to the cavity have a different radius to those in the 'bulk' of the photonic crystal. The radius and separation of these 'modified' holes are also varied in the optimization routine. The first stage of the simulation process is to calculate the photonic band-gap structure, shown in figure 19. This gives a starting point for optimizing the lattice constants and hole radii. Figure 20 shows the electromagnetic field profiles

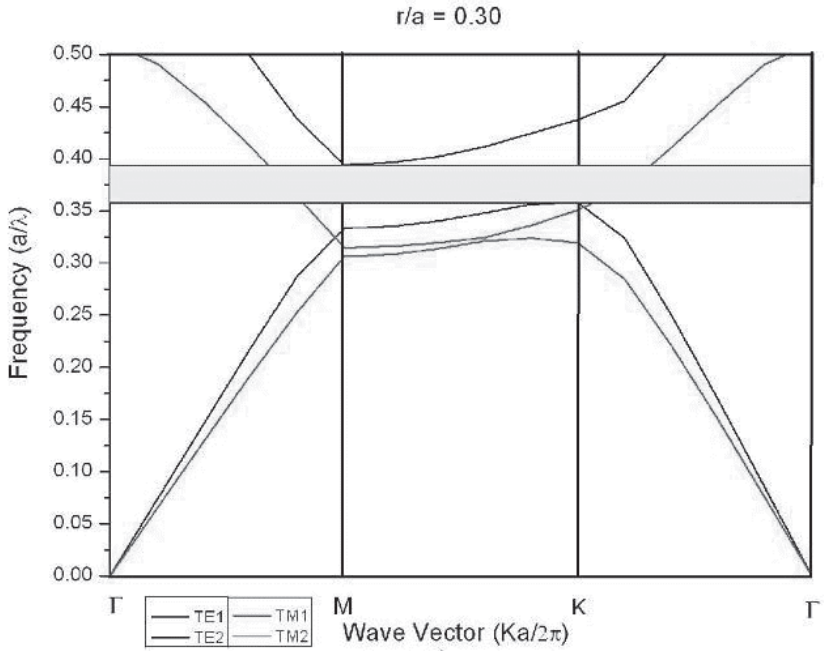

Figure 19. Photonic band-gap structure calculated from the simulation.

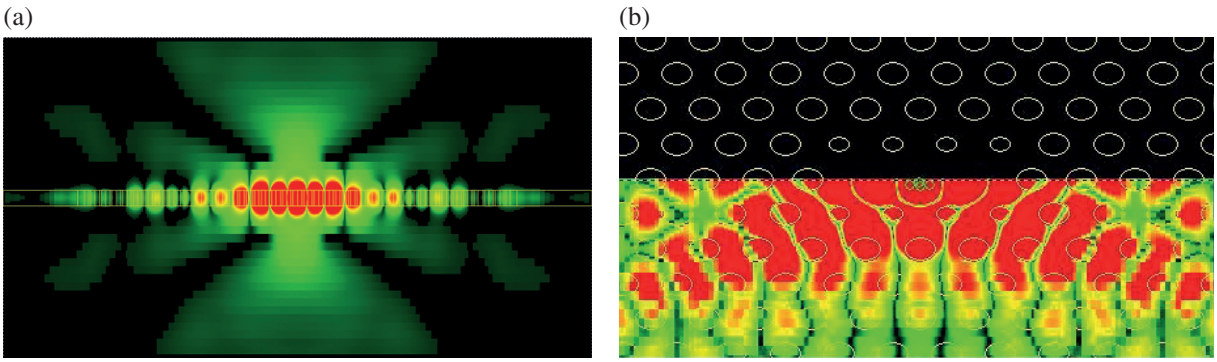

Figure 20. Electromagnetic field profiles calculated in FDTD simulations. (a) View in the plane of the suspended slab. (b) View looking down on the cavity.

calculated in the simulations. From the simulations we calculate the decaying oscillation of the electromagnetic field inside the cavity (figure 21(a)). Taking the Fourier transform of this signal, the cavity Q can then be calculated (figure 21(b)). After optimization, the best Q-factor obtained in the simulations was 3.2×10^4.

3.1.2. Fabrication. Photonic crystal cavities in diamond were fabricated using the FIB apparatus described in section 2.1.2. In the first fabrication step, the diamond crystal is undercut by turning side-on and etching to obtain a 200 nm thick slab attached to the bulk. The diamond is then re-positioned so that the air holes can be etched in this suspended slab (figure 22). These cavities, etched in ultra-pure diamond material (Element Six), have been scanned in our confocal microscope system. Enhanced background fluorescence from etch damage is seen in

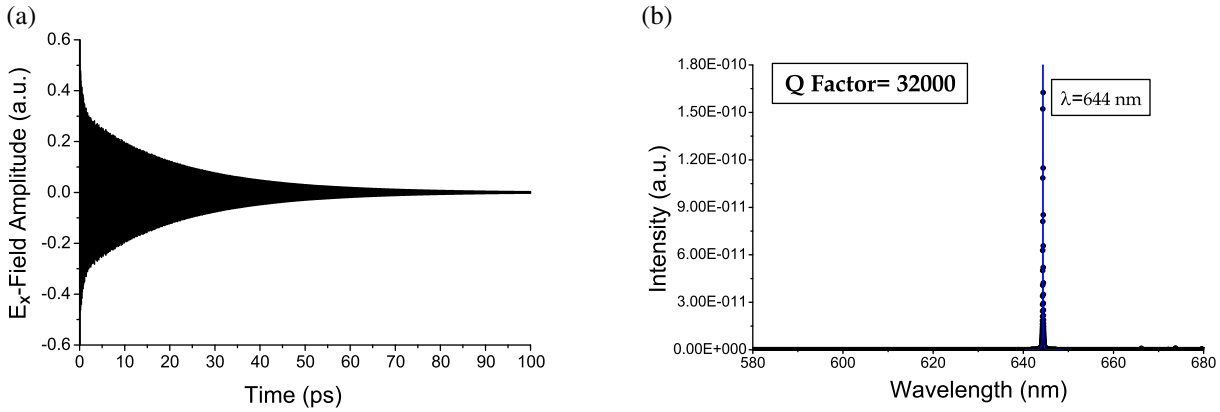

Figure 21. Electromagnetic field amplitude calculated in FDTD simulations. (a) Time dependence of the electromagnetic field inside the cavity and (b) Fourier transform of the decay signal.

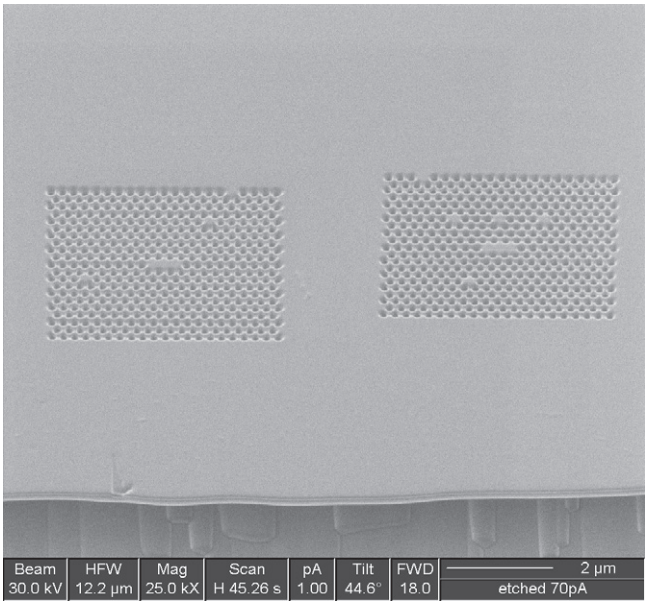

Figure 22. Photonic crystal fabricated in ultra-high-purity diamond. Image is taken using secondary electron emission in FIB.

the areas where holes are etched, while reduced background is seen in the cavity region. As yet we have not seen any narrow spectral features in the background light from the cavity region which could be associated with high-Q resonances. However, Q-factors below 100 are not ruled out by data taken to date. We are at present assessing the possibility of making un-etched cavity regions that are much larger and/or simpler cavity structures.

4. Conclusions

Diamond has much to offer the emerging field of quantum information processing. The presence of bright color centers with unique quantum properties makes diamond an extremely promising

platform for solid-state quantum computing using photons as flying qubits. However, the sculpting of diamond at the nanoscale is exceedingly difficult and relatively immature compared with more conventional photonic media. We have described the progress towards several important diamond structures for the collection and routing of fluorescence from NV^- centers. These include SILs, photonic crystal cavities and waveguides. Some of the more important failure mechanisms associated with milling structures in diamond were discussed, along with progress towards their mitigation. Most importantly, we outlined some of the progress to transition diamond fabrication from one-off devices, to taking advantage of industry-standard techniques for parallel fabrication via photolithography and RIE. Ultimately, leveraging mature photonics fabrication techniques to develop a full diamond nanofabrication toolkit will be essential if diamond is to realize its promise as the material of choice for solid-state quantum information processing.

Acknowledgments

This work was supported by the European Union's Sixth Framework Program under EQUIND IST-034368 and by the Australian Research Council, the International Science Linkages Program of the Australian Department of Innovation, Industry, Science and Research (project no. CG110039). BCG and STH acknowledge support from the International Science Linkages program established under the Australian Government's innovation statement Backing Australia's Ability. The authors also acknowledge the Victorian Government's Science, Technology and Innovation Infrastructure Grants Program. ADG is the recipient of an Australian Research Council Queen Elizabeth II Fellowship (project no. DP0880466). JGR is supported by a Wolfson Research Merit Award. The authors acknowledge Professors Railton and Craddock from the Department of Electrical and Electronic Engineering, University of Bristol, for the development of the FDTD codes used in this work.

References

[1] Beveratos A, Brouri R, Gacoin T, Villing A, Poizat J P and Grangier P 2002 Single photon quantum cryptography *Phys. Rev. Lett.* **89** 187901
[2] Gaebel T *et al* Room-temperature coherent coupling of single spins in diamond *Nat. Phys.* **2** 408
[3] Childress L, Gurudev Dutt M V, Taylor J M, Zibrov A S, Jelezko F, Wrachtrup J, Hemmer P R and Lukin M D 2006 Coherent dynamics of coupled electron and nuclear spin qubits in diamond *Science* **314** 281
[4] Balasubramanian G *et al* 2008 Nanoscale imaging magnetometry with diamond spins under ambient conditions *Nature* **455** 648
[5] Rittweger E, Han K Y, Irvine S E, Eggeling C and Hell S W 2009 STED microscopy reveals crystal colour centres with nanometric resolution *Nat. Photonics* **3** 144
[6] Kurtsiefer C, Mayer S, Zarda P and Weinfurter H 2000 Stable solid-state source of single photons *Phys. Rev. Lett.* **85** 290
[7] Hanson R, Mendoza F M, Epstein R J and Awschalom D D 2006 Polarization and readout of coupled single spins in diamond *Phys. Rev. Lett.* **97** 087601
[8] Jelezko F, Gaebel T, Popa I, Domhan M, Gruber A and Wrachtrup J 2004 Observation of coherent oscillation of a single nuclear spin and realization of a two-qubit conditional quantum gate *Phys. Rev. Lett.* **93** 130501
[9] Neumann P, Mizuochi N, Rempp F, Hemmer P, Watanabe H, Yamasaki S, Jacques V, Gaebel T, Jelezko F and Wrachtrup J 2008 Multipartite entanglement among single spins in diamond *Science* **320** 1326
[10] Quantum Communications Victoria, http://qcvictoria.com

[11] Balasubramanian G *et al* 2009 Ultralong spin coherence time in isotopically engineered diamond *Nat. Mater.* **8** 383
[12] Santori C, Pelton M, Solomon G, Dale Y and Yamamoto Y 2001 Triggered single photons from a quantum dot *Phys. Rev. Lett.* **86** 1502
[13] Stephens A M, Evans Z W E, Devitt S J, Greentree A D, Fowler A G, Munro W J, OBrien J L, Nemoto K and Hollenberg L C L 2008 Deterministic optical quantum computer using photonic modules *Phys. Rev.* A **78** 032318
[14] van der Sar T, Heeres E C, Dmochowski G M, de Lange G, Robledo L, Oosterkamp T H and Hanson R 2009 Nanopositioning of a diamond nanocrystal containing a single nitrogen-vacancy defect center *Appl. Phys. Lett.* **94** 173104
[15] Ampem-Lassen E, Simpson D A, Gibson B C, Trpkovski S, Hossain F M, Huntington S T, Ganesan K, Hollenberg L C L and Prawer S 2009 Nano-manipulation of diamond-based single photon sources *Opt. Express* **17** 11287
[16] Barth M, Nüsse N, Löchel B and Benson O 2009 Controlled coupling of a single-diamond nanocrystal to a photonic crystal cavity *Opt. Lett.* **34** 1108
[17] Schröder T, Schell A W, Kewes G, Aichele T and Benson O 2010 Fiber-integrated diamond-based single photon source *Nano Lett.* **11** 198–202
[18] Fu K M, Santori C, Barclay P E, Aharonovich I, Prawer S, Meyer N, Hold A M and Beausoleil R G 2008 Coupling of nitrogen-vacancy centers in diamond to a GaP waveguide *Appl. Phys. Lett.* **93** 234107
[19] Park Y S, Cook A K and Wang H 2006 Cavity QED with diamond nanocrystals and silica microspheres *Nano Lett.* **6** 2075–9
[20] Barclay P E, Santori C, Fu K-M, Beausoleil R G and Painter O 2009 Coherent interference effects in a nano-assembled diamond NV center cavity-QED system *Opt. Express* **17** 8081
[21] Barclay P E, Fu K-M C, Santori C and Beausoleil R G 2009 Chip-based microcavities coupled to nitrogen-vacancy centers in single crystal diamond *Appl. Phys. Lett.* **95** 191115
[22] Hiscocks M P, Ganesan K, Gibson B C, Huntington S T, Ladouceur F and Prawer S 2008 Diamond waveguides fabricated by reactive ion etching *Opt. Express* **16** 19512
[23] Babinec T M, Hausmann B J M, Khan M, Zhang Y, Maze J R, Hemmer P R and Loncar M 2010 A diamond nanowire single-photon source *Nat. Nanotechnol.* **5** 195
[24] Su C H, Greentree A D and Hollenberg L C L 2008 Towards a picosecond transform-limited nitrogen-vacancy based single photon source *Opt. Express* **16** 6240
[25] Schietinger S, Schröder T and Benson O 2008 One-by-one coupling of single defect centers in nanodiamonds to high-Q modes of an optical microresonator *Nano Lett.* **8** 3911
[26] Hiscocks M P, Su C H, Gibson B C, Greentree A D, Hollenberg L C L and Ladouceur F 2009 Slot-waveguide cavities for optical quantum information applications *Opt. Express* **17** 7295–303
[27] Tomljenovic-Hanic S, Steel M J, Martijn de Sterke C and Salzman J 2006 Diamond based photonic crystal microcavities *Opt. Express* **14** 3556
[28] Tomljenovic-Hanic S, Greentree A D, de Sterke C M and Prawer S 2009 Flexible design of ultrahigh-Q microcavities in diamond-based photonic crystal slabs *Opt. Express* **17** 6465
[29] Bayn I and Salzman J 2007 High-Q photonic crystal nanocavities on diamond for quantum electrodynamics *Eur. Phys. J. Appl. Phys.* **37** 19
[30] Bayn I, Meyler B, Lahav A, Salzman J, Fairchild B A, Prawer S and Martinez F L 2008 Photonic crystals (PC) in diamond: ultra-high-Q nanocavity design, analysis and fabrication *Proc. 14th European Conf. on Integrated Optics and Technical Exhibition* (*Eindhoven*)
[31] Wang C F, Choi Y S, Lee J C, Hu E L, Yang J and Butler J E 2007 Observation of whispering gallery modes in nanocrystalline diamond microdisks *Appl. Phys. Lett.* **90** 081110
[32] Wang C F, Hanson R, Awschalom D D, Hu E L, Feygelson T, Yang J and Butler J E 2007 Fabrication and characterization of two-dimensional photonic crystal microcavities in nanocrystalline diamond *Appl. Phys. Lett.* **91** 201112

[33] Fairchild B A *et al* 2008 Fabrication of ultrathin single-crystal diamond membranes *Adv. Mater.* **20** 4793
[34] Young A, Hu C Y, Marseglia L, Harrison J P, O'Brien J L and Rarity J G 2009 Cavity enhanced spin measurement of the ground state spin of an NV center in diamond *New J. Phys.* **11** 013007
[35] Beveratos A, Kühn S, Brouri R, Gacoin T, Poizat J P and Grangier P 2002 Room temperature stable single-photon source *Eur. Phys. J.* D **18** 191
[36] Meijer J, Burchard B, Domham M, Wittmann C, Gaebel T, Popa I, Jelezko F and Wrachtrup J 2005 Generation of single color centers by focused nitrogen implantation *Appl. Phys. Lett.* **87** 261909
[37] Jamieson D N *et al* 2005 Controlled shallow single-ion implantation in silicon using an active substrate for sub-20-keV ions *Appl. Phys. Lett.* **86** 202101
[38] Meijer J *et al* 2008 Towards the implantating of ions and positioning of nanoparticles with nm spatial resolution *Appl. Phys.* A **91** 567
[39] Mansfield S M and Kino G S 1990 Solid immersion microscope *Appl. Phys. Lett.* **57** 2615
[40] Sasaki T, Motoyoshi B, Yoshita M and Akiyama H 1997 Application of solid immersion lens to high-resolution photoluminescence imaging of patterned GaAs quantum wells *Japan J. Appl. Phys.* **36** L962
[41] Wu Q, Feke G D, Grober R D and Ghislain L P 1999 Realization of numerical aperture 2.0 using a gallium phosphide solid immersion lens *Appl. Phys. Lett.* **75** 4064
[42] Schröder T, Gädeke F, Banholzer M J and Benson O 2010 Ultra-bright and efficient single photon generation based on N-V centres in nanodiamonds on a solid immersion lens arXiv:1011.1822
[43] Hadden J P, Harrison J P, Stanley-Clark A C, Marseglia L, Ho Y L D, Patton B R, O'Brien J L and Rarity J G 2010 Strongly enhanced photon collection from diamond defect centers under microfabricated integrated solid immersion lenses *Appl. Phys. Lett.* **97** 241901
[44] Barnes W L, Björk G, Gérard J M, Jonsson P, Wasey J A E, Worthing P T and Zwiller V 2002 Solid-state single photon sources: light collection strategies *Eur. Phys. J.* D **18** 197
[45] Marseglia L *et al* 2010 Nano-fabricated solid immersion lenses registered to single emitters in diamond arXiv:1012.1135
[46] Aharonovich I, Castelletto S, Simpson D A, Stacey A, McCallum J, Greentree A D and Prawer S 2009 Two-level ultra bright single photon emission from diamond nanocrystals *Nano Lett.* **9** 3191–5
[47] Aharonovich I, Castelletto S, Brett Johnson C, McCallum J C, Simpson D A, Greentree A D and Prawer S 2010 Chromium single-photon emitters in diamond fabricated by ion implantation *Phys. Rev.* B **81** 121201
[48] Olivero P *et al* 2005 Ion-beam-assisted lift-off technique for three-dimensional micromachining of freestanding single-crystal diamond *Adv. Mater.* **17** 2427
[49] Parikh N R, Hunn J D, McGucken E, Swanson M L, White C W, Rudder R A, Malta D P, Posthill J B and Markunas R J 1992 *Appl. Phys. Lett.* **61** 3124
[50] Uzan-Saguy C, Cytermann C, Brener R, Richter V, Shaanan M and Kalish R 1995 Damage threshold for ion-beam induced graphitization of diamond *Appl. Phys. Lett.* **67** 1194
[51] Orwa J O, Nugent K W, Jamieson D N and Prawer S 2000 *Phys. Rev.* B **62** 5461
[52] Hickey D P, Jones K S and Elliman R G 2009 *Diam. Relat. Mater.* **18** 1353
[53] Rubanov S, Munroe P, Prawer S and Jamieson D 2003 Surface damage in silicon after 30 keV Ga FIB fabrication *Microsc. Microanal.* **9** 884
[54] Tseng A A *et al* 2004 *J. Micromech. Microeng.* **14** r14.0
[55] Orbons S M, Dijk L V, Bozkurt M, Johnston P N, Reichart P and Jamieson D N 2006 *Nucl. Instrum. Methods Phys. Res.* B **249** 747
[56] Olivero P, Rubanov S, Reichart P, Gibson B C, Huntington S T, Rabeau J, Greentree A D, Salzman J, Moore D, Jamieson D N and Prawer S 2006 Characterization of three-dimensional microstructures in single-crystal diamond *Diam. Relat. Mater.* **15** 1614
[57] Draganski M A *et al* 2008 The refractive index of ion implanted diamond *Proc. 18th Australian Institute of Physics (AIP) National Congress (The University of South Australia, 30 November–5 December)* p 133
[58] Giannuzzi L A and Stevie F A 1999 A review of focused ion beam milling techniques for TEM specimen preparation *Micron* **30** 197

[59] Hiscocks M P, Kaalund C J, Ladouceur F, Huntington S T, Gibson B C, Trpkovski S, Simpson D, Ampem-Lassen E, Prawer S and Butler J E 2008 Reactive ion etching of waveguide structures in diamond *Diam. Relat. Mater.* **17** 1831

[60] Karlsson M and Nikolajeff F 2003 Diamond micro-optics: microlenses and antireflection structured surfaces for the infrared spectral region *Opt. Express* **11** 502

[61] Enlund J, Isberg J, Karlsson M, Nikolajeff F, Olsson J and Twitchen D J 2005 Anisotropic dry etching of boron doped single crystal CVD diamond *Carbon* **43** 1839

[62] Joannopoulous J D, Meade R D and Winn J N 1995 *Photonic Crystals: Molding the Flow of Light* (Princeton, NJ: Princeton University Press)

[63] Zhang Z and Qiu M 2004 Small-volume waveguide-section high Q microcavities in 2D photonic crystal slabs *Opt. Express* **12** 3988